Janus effect of antifreeze proteins on ice nucleation

Kai Liu[a,b], Chunlei Wang[c,1], Ji Ma[d], Guosheng Shi[c], Xi Yao[a], Haiping Fang[c], Yanlin Song[a,b], and Jianjun Wang[a,b,1]

[a]Key Laboratory of Green Printing, Institute of Chemistry, Chinese Academy of Sciences, Beijing 100190, People's Republic of China; [b]School of Chemistry and Chemical Engineering, University of Chinese Academy of Sciences, Beijing 100049, People's Republic of China; [c]Division of Interfacial Water and Key Laboratory of Interfacial Physics and Technology, Shanghai Institute of Applied Physics, Chinese Academy of Sciences, Shanghai 201800, People's Republic of China; and [d]Xinjiang Key Laboratory of Biological Resources and Genetic Engineering, College of Life Science and Technology, Xinjiang University, Urumqi 830046, People's Republic of China

Edited by Pablo G. Debenedetti, Princeton University, Princeton, NJ, and approved November 17, 2016 (received for review August 29, 2016)

The mechanism of ice nucleation at the molecular level remains largely unknown. Nature endows antifreeze proteins (AFPs) with the unique capability of controlling ice formation. However, the effect of AFPs on ice nucleation has been under debate. Here we report the observation of both depression and promotion effects of AFPs on ice nucleation via selectively binding the ice-binding face (IBF) and the non–ice-binding face (NIBF) of AFPs to solid substrates. Freezing temperature and delay time assays show that ice nucleation is depressed with the NIBF exposed to liquid water, whereas ice nucleation is facilitated with the IBF exposed to liquid water. The generality of this Janus effect is verified by investigating three representative AFPs. Molecular dynamics simulation analysis shows that the Janus effect can be established by the distinct structures of the hydration layer around IBF and NIBF. Our work greatly enhances the understanding of the mechanism of AFPs at the molecular level and brings insights to the fundamentals of heterogeneous ice nucleation.

antifreeze proteins | ice nucleation | Janus effect | interfacial water | selective tethering

Antifreeze proteins (AFPs) protect a broad range of organisms inhabiting subzero environments. The function of AFPs lies in lowering the freezing point in a noncolligative manner (1, 2). It has been shown that AFPs can adsorb on the ice crystal surface with the ice-binding face (IBF, also termed ice-binding site or ice-binding surface) (3, 4). The adsorbed AFPs lead to curvatures on the ice surface between adjacent AFPs, and ice growth is retarded due to the Kelvin effect, which is known as the adsorption–inhibition mechanism (5). However, whether the non–ice-binding face (NIBF) is involved in the function of AFPs and what effect the NIBF exerts are rarely studied (4, 6, 7). On the other hand, the effect of AFPs on ice nucleation (8) is still under intense debate (9–13), although ice nucleation, the formation of a stable nucleus with a critical size, is the control step for ice formation (8). Liu et al. (9) suggested that AFPs could inhibit heterogeneous ice nucleation of water, whereas research on ice nucleation of microdroplets of AFP solutions exhibited no obvious effect of AFPs in inhibiting ice nucleation (10). It was also reported that an AFP solution with high concentration facilitated ice nucleation (11). The contradiction also exists for the research of ice nucleation on solid surfaces immobilized with AFPs (12, 13). Therefore, it is highly desirable to elucidate the exact role of AFPs on ice nucleation and to correlate AFP structures at the molecular level with their function in tuning ice nucleation, which is essential for practical applications in food, pharmaceutical, and chemical industries (14, 15).

Herein, we investigate the effect of IBF and NIBF of AFPs on ice nucleation via binding AFPs to solid substrates in a way that either IBF or NIBF is exposed to liquid water. This binding method is readily extendable to other AFPs because of the clear distinction between IBF and NIBF; and IBFs of AFPs are relatively flat and often have a regular array of hydroxyl groups in comparison with the NIBFs (16, 17). The results reveal that the IBF of AFPs facilitates ice nucleation, whereas the NIBF depresses ice nucleation. This Janus effect of AFPs is general because it is observed on three representative AFPs, i.e., a hyperactive insect AFP from the beetle *Microdera punctipennis dzungarica* (*Mpd*AFP), a bacterial AFP from *Marinomonas primoryensis* (*Mp*AFP), and a moderate active fish AFP (type III AFP). Molecular dynamics (MD) simulation analysis reveals that water molecules on the IBF form ice-like interfacial water structure due to the special arrangement of hydrophobic methyl and hydrophilic hydroxyl groups on the IBF. In strong contrast, almost no ice-like water structure is formed on the NIBF, which is possibly due to the absence of regular hydrophobic/hydrophilic patterns as well as the existence of charged groups and bulky hydrophobic groups (6). Therefore, a molecular level understanding of AFPs in tuning ice nucleation is established. Most importantly, our work provides a comprehensive picture of the effect of AFPs on ice nucleation, which will certainly guide materials scientists to design and synthesize biomimetic compounds for regulating ice nucleation.

Results

Selectively Tethering IBF and NIBF of AFPs to Solid Substrates. An AFP from *M. p. dzungarica* (*Mpd*AFP) (Fig. 1*A*), a beetle inhabiting Xinjiang, an autonomous region of China, was first expressed and investigated (Fig. S1) (18). This insect AFP shares 77% similarity in the residual sequence with antifreeze protein of *Tenebrio molitor* (*Tm*AFP) (17, 19). *Mpd*AFP is also composed of tandem 12-amino acid repeats (TCTxSxxCxxAx) (Fig. S2). The modeled structure of *Mpd*AFP in Fig. 1*A* displays a flattened cylinder with a pseudorectangular cross-section. The most prominent feature of the *Mpd*AFP is that threonine–cysteine–threonine (TCT) motifs are arrayed to constitute a flat β-sheet face with the threonine residues projecting outward in two aligned parallel arrays, which form the IBF of the *Mpd*AFP. Our investigations on the ice crystal shaping and thermal hysteresis (TH) values (Fig. S3) clearly show that *Mpd*AFP is a typical hyperactive AFP (20). One important feature

Significance

In the past decades, a vast body of experimental and theoretical work has been undertaken to investigate the molecular level mechanism underlying heterogeneous ice nucleation. However, understanding of heterogeneous ice nucleation is still far from satisfactory. Antifreeze proteins (AFPs) are endowed with the unique ability to control freezing. Our research reveals the exact effect of AFPs on ice nucleation at the molecular level, which correlates ice nucleation with the surface chemistry and topography of different faces of AFPs. We also emphasize a critical role for the non–ice-binding face of AFPs and discover that the proper function of AFPs is realized only by synergistic effects of the non–ice-binding face and the ice-binding face.

Author contributions: J.W. designed research; K.L. and C.W. performed research; J.M. contributed new reagents/analytic tools; K.L. and C.W. analyzed data; and K.L., C.W., J.M., G.S., X.Y., H.F., Y.S., and J.W. wrote the paper.

The authors declare no conflict of interest.

This article is a PNAS Direct Submission.

[1]To whom correspondence may be addressed. Email: wangj220@iccas.ac.cn or wangchunlei@sinap.ac.cn.

This article contains supporting information online at www.pnas.org/lookup/suppl/doi:10.1073/pnas.1614379114/-/DCSupplemental.

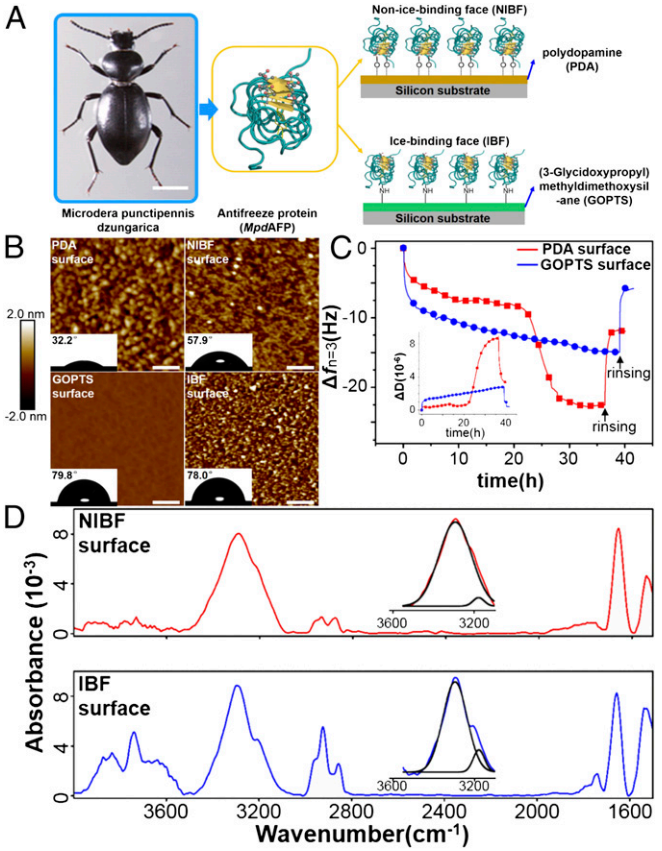

Fig. 1. Characterization of tethered *Mpd*AFPs on PDA and GOPTS surfaces. (*A*) Illustration of antifreeze protein from an insect (*M. p. dzungarica*) and selectively tethered *Mpd*AFPs on the PDA and GOPTS surfaces. (Scale bar in the photograph of *M. p. dzungarica*, 1 cm.) (*B*) The atomic force microscope images of PDA surface, NIBF surface, GOPTS surface, and IBF surface in the size of 500 × 500 nm, respectively. (Scale bar, 100 nm.) The NIBF surface and the IBF surface show almost the same roughness. The static contact angle data of four kinds of surfaces in the *Insets* manifest the major difference of NIBF surface and IBF surface due to the selective immobilization of *Mpd*AFPs. (*C*) QCM-D investigates the frequency change during the immobilization of *Mpd*AFPs on the PDA and GOPTS surfaces and the *Inset* is the dissipation change, which verifies that bonding of proteins immobilized on two surfaces are completely different. (*D*) The ATR-FTIR spectroscopy of *Mpd*AFPs on the PDA and GOPTS surfaces. The presence or absence of the absorbance at 3,700 cm^{-1} due to the free hydroxyl group displays the success of selective tethering *Mpd*AFP on two kinds of surfaces. *Insets* show the residual water absorbance from 3,150 cm^{-1} to 3,600 cm^{-1}, indicating more ice-like bound waters on the IBF surface.

of AFPs should be noted, which is, AFPs are a type of protein interacting with solid surfaces (e.g., ice crystals), which suggests that AFPs can be immobilized on solid surfaces without denaturing and thus loss of antifreeze activity.

We used dopamine (DA), a low-molecular weight mimic of the adhesive protein secreted by marine mussels (21) as a binder to immobilize AFPs. After polymerization of DA on solid substrates, polydopamine (PDA) film with large amounts of hydroxyl groups binds the IBF of AFPs via multiple hydrogen bonds with the hydroxyl groups at the threonines (22) and then the NIBF is exposed outward (NIBF surface). On the other hand, we used (3-glycidoxypropyl) methyldimethoxysilane (GOPTS) to bind the primary amine groups of N-terminal and lysines at the NIBF, which are absent at the IBF of AFPs. Then the surface with IBF exposed (IBF surface) was obtained. Fig. 1*A* schematically illustrates the orientation of *Mpd*AFPs on the PDA-modified surfaces and the GOPTS-modified surfaces (detailed protocols in Fig. S4).

The atomic force microscopy (AFM) (Fig. 1*B*) and X-ray photoelectron spectroscopy (XPS) (Fig. S5) investigations verify the successful immobilization of *Mpd*AFPs on two surfaces, as indicated by the variations of the roughness and surface morphology as well as the nitrogen to carbon (N/C) ratio before and after the modification. The roughness of the PDA surface was 0.520 nm, and the roughness became 0.445 nm after the modification, whereas the roughness of the GOPTS surface was 0.030 nm, and it increased to 0.482 nm after the proteins modification. The corresponding contact angles of water droplets on these surfaces are shown in the *Insets* of Fig. 1*B*. The contact angle increases from 32.2° to 57.9° when the PDA surface is tethered with *Mpd*AFPs, whereas the contact angle decreases slightly from 79.8° to 78.0° when the GOPTS surface is tethered with *Mpd*AFPs. The difference between the values of the contact angles on the NIBF and IBF surfaces could be reconciled when one considers the fact that the IBF is more hydrophobic than the NIBF of AFPs (3), which indicates that selective tethering has been achieved. Selective tethering was consolidated by monitoring the tethering process with quartz crystal microbalance with dissipation monitoring (QCM-D), where the variation of frequency (*F*) and dissipation (*D*) in the process of tethering the AFPs on the PDA and GOPTS shows completely different behavior (Fig. 1*C*). This finding proves the different orientation of AFPs on the PDA surface and the GOPTS surface, respectively. (Details of the analysis can be found in *SI Text*).

We then used attenuated total reflectance Fourier transform infrared spectroscopy (ATR-FTIR) to verify the success of PDA and GOPTS in selectively anchoring the IBF and NIBF of the *Mpd*AFP. As shown in Fig. 1*D*, NIBF and IBF surfaces share the same absorbance of amide I band around 1,640 cm^{-1} and the amide II band around 1,550 cm^{-1}, which means that the *Mpd*AFPs maintained the conformation after being tethered on the solid substrates (23). The selective tethering of AFPs on the PDA and GOPTS surfaces is obvious as signified by the presence and absence of the absorbance of free hydroxyl groups (24) around 3,700 cm^{-1}. It is shown that the IBF with multiple hydroxyl groups of threonine arrays exposed outward on the GOPTS surface, whereas the IBF attached to surfaces by binding multiple hydroxyl groups of two threonine arrays to the PDA surface and the NIBF is exposed outward. The *Insets* of Fig. 1*D* show the peak fitting for the absorbance in the range from 3,150 cm^{-1} to 3,600 cm^{-1}, which might contain information of bound water molecules on the surfaces. The absorbance around 3,200 cm^{-1} of the IBF surface is stronger, which suggests that there are more ice-like waters on the IBF surface (25). It should be caused by the exposed IBF on the GOPTS surface, on which the regular arrangement of functional groups on IBF organizes bound waters to have an ice-like structure (26).

Effect of IBF and NIBF Surfaces on Ice Nucleation. Freezing of water droplets (0.1 μL) on various surfaces was investigated in a closed cell to ensure a constant relative humidity of 100% (Fig. S6). The freezing of droplets was monitored with a high speed camera coupled to an optical microscope. Fig. 2*A* shows a typical freezing process of a water droplet in a closed cell. The freezing was observed to initiate near the liquid/solid interface and then grew rapidly along that plane. Because the temperature of the droplet is lowered by the cryostage beneath, it is safe to say that ice nucleation started at the liquid/solid interface, which was also reported by another research group (27). The rapid growth of ice along the liquid/solid interface should be due to the better thermal conductivity of the silicon substrate and the released latent heat could be quickly removed (28) (Movie S1). The ice grew upward when the substrate was entirely covered with ice, whereas the growth rate was much lower than that along the liquid/solid interface (Movie S1). The air/water interface became rougher when it turned to an air/ice interface and the upward propagation of the resulting rough surface can be clearly seen when the freezing occurred. Fig. 2*A*, *Lower* schematically illustrates the freezing process of the droplet

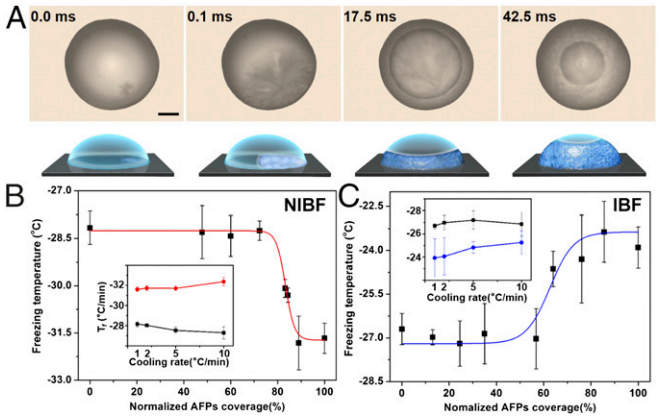

Fig. 2. Ice nucleation on the NIBF and IBF surfaces. (*A*) *Upper* images show the representative images taken by a high-speed camera coupled to an optical microscope, which monitors the freezing of droplets on the NIBF and IBF surfaces; these images show that ice nucleation occurs at the liquid/solid interface, and then ice grows along the liquid/solid interface first and then grows upward. (Scale bar, 200 μm.) *Lower* images are the schematic illustration of the freezing process corresponding to the *Upper* set. (*B* and *C*) Effects of the NIBF surface and IBF surface on ice nucleation. Fig. 3 *B* and *C*, *Insets* show the ice nucleation temperature of the fully covered NIBF surface and IBF surface under different cooling rates, respectively, confirming that the NIBF surface depresses the formation of the stable ice nucleus and the IBF surface facilitates the formation of ice nucleus. We investigated freezing events of about 100 individual water droplets and applied the Gaussian fitting to get mean values and SD.

initiating at the liquid/solid interface and then propagating upward. As the nucleation starts at the liquid/solid interface, the effects of AFPs on ice nucleation can be reliably investigated when AFPs are tethered to solid substrates. QCM-D was used to verify that there were no AFPs dissolved into water when the AFP-modified surface was in contact with liquid water droplets during the investigation for ice nucleation (Fig. S7).

To quantitatively characterize the effects of NIBF and IBF on ice nucleation, we explored the nucleation temperature against the surface coverage of AFPs. According to our QCM-D results, the surface coverage of AFPs can be tuned by changing the modified time of AFPs on PDA and GOPTS surfaces (Fig. S8) (details of the analysis in *SI Text*). The average ice nucleation temperature on NIBF surfaces with different AFP coverage was investigated at a cooling rate of 5 °C/min (Fig. 2*B*). The mean value and SD of ice nucleation temperatures were obtained based on independent ice nucleation events on about 100 different locations via Gaussian fitting (Fig. S9). When the surface coverage of AFP was lower than about 80.0%, the nucleation temperature was around −28.0 °C, the same as that on the PDA surface, demonstrating that NIBF has little effect on ice nucleation when the coverage is below 80.0%. However, the nucleation temperature showed a sharp decrease when the surface coverage was larger than 80.0%. It saturated above the surface coverage of 90.0% with the nucleation temperature being −31.9 °C. Fig. 2*B*, *Inset* shows the nucleation temperature with various cooling rates on the PDA surface fully covered with NIBF, which confirms that the NIBF of the *Mpd*AFP depresses ice nucleation.

In sharp contrast, ice nucleation on IBF surfaces was facilitated (Fig. 2*C*). When the surface coverage of AFPs was lower than 64.0%, ice nucleation on these surfaces occurred around −27.5 °C. When the coverage increased above 64.0%, ice nucleation temperature increased sharply and then reached a plateau at around −23.0 °C when the surface coverage went higher than 80.0%. Our results indicate an increase of ice nucleation temperature about 4.5 °C on the IBF surfaces. Fig. 2*C*, *Inset* demonstrates that at various cooling rates, the ice nucleation temperature on the surfaces fully covered with IBFs remains higher than that on the GOPTS surface. For supercooled liquid water, ice nucleation of a droplet initiates at the most active site, and then ice grows spontaneously (29). Thus, to achieve lower ice nucleation temperature, it is required to sufficiently minimize the amount of nucleation active sites in contact with liquid water. Experimental results show that it takes 80.0% of the AFP coverage on the PDA surface for the depression of nucleation to occur. On the other hand, it would be possible that the IBF cluster domain size should reach a critical value for the occurrence of nucleation promotion, which based on our experimental results, can be interpreted as 64.0% of the AFP coverage on the GOPTS surface. Facilitating ice nucleation with IBF clusters of specific domain size is reminiscent of the ice nucleation protein (INP), which is believed to be a larger version of AFPs and can promote ice nucleation greatly (30).

The Janus effect of AFPs in tuning ice nucleation was consolidated by the delay time assay of ice nucleation, which was measured by fixing a specific supercooling temperature and then recording the time needed for ice nucleation to occur. Ice nucleation occurs on the PDA surface and NIBF surface at around 25 s and 2,254 s, respectively, with a surface temperature of −28.0 °C in a closed chamber with a relative humidity of 100% (Fig. 3*A*). The delay time of nucleation on the NIBF surface is almost two orders of magnitude longer than that on the PDA surface. Ice nucleation occurred at 8 s on the IBF surface and at 1,185 s on the GOTPS surface with a surface temperature of −24.0 °C, verifying the fact that the IBF of *Mpd*AFPs enhances ice nucleation (Fig. 3*B*).

We also examined the generality of the Janus effect of AFPs on ice nucleation. The other two types of AFPs, *Mp*AFP (31) and type III AFP from the polar fish eelpout (16) have been investigated. We used the same tethering method to bind *Mp*AFP and type III AFP to solid substrates. When the NIBF of the *Mp*AFP or type III AFP was exposed to liquid water, it showed a decreased ice nucleation temperature. The difference of the nucleation temperature with that of the PDA surface is on average 0.03 °C and 4.19 °C for type III AFP and *Mp*AFP, respectively (Fig. S9). On the other hand, when the IBF of the *Mp*AFP and type III AFP was exposed to the liquid water, an increased nucleation temperature was observed. The difference of ice nucleation temperature with that of the GOPTS surface is on average 0.18 °C and 3.21 °C for type III AFP and *Mp*AFP, respectively (Fig. S9). In conclusion, AFPs of different species exhibit the same Janus effect on ice nucleation. We

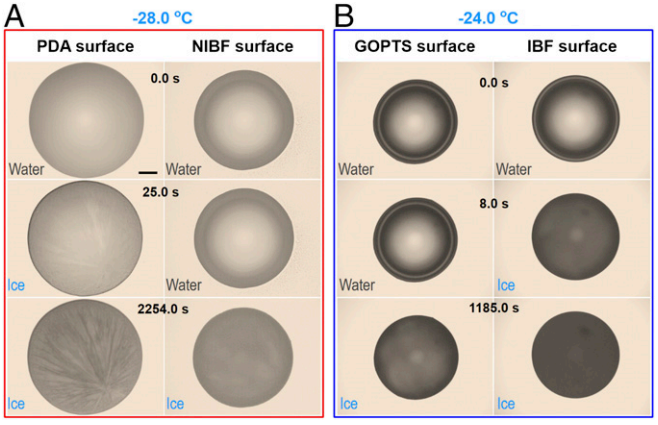

Fig. 3. The delay time measurement for freezing of supercooled droplets. (*A*) On the NIBF surface in comparison with that on the PDA surface and (*B*) IBF surface in comparison with that on the GOPTS surface. (Scale bar, 200 μm.) The NIBF and IBF surfaces used correspond to the sample of 100% normalized AFP coverage. The temperature was set according to the freezing temperature assay to make sure that an ice nucleation event would not occur until the set temperature was reached. The cooling rate is 5 °C/min.

have discovered with interest a correlation between the activity of three AFPs on ice nucleation and that on TH, i.e., moderate active AFPs exhibit lower activities both in facilitating and depressing ice nucleation, and hyperactive AFPs show higher activities in facilitating and depressing ice nucleation (Fig. S10).

Molecular Level Mechanism of AFPs in Tuning Ice Nucleation. The structure of the hydration waters on the solid surfaces is usually the key in determining the surface properties (32–35). So we carried out MD simulation to investigate the structure of the water molecules atop the IBF and NIBF of *Tm*AFP (Fig. S11). Here *Tm*AFP was chosen due to its well-established structure and its high homology to *Mpd*AFP (17, 19). We note that the direct simulation of ice nucleation is still an intimidating challenge due to the extremely large computational costs (8, 36, 37). We therefore use the preexisting ice that grows and passes through the AFP, which can give the molecular-level information of interplay between ice and the AFP. For three independent simulations, we observed ordered water structures atop the IBF and disordered water structures atop the NIBF. Fig. 4*A* shows a typical side view snapshot of one trajectory with water molecules atop the IBF, and Fig. 4*B* shows the top view. It is obvious that hexagonal ice-like structure (38) with a hexagonal hydrogen bond network formed atop the IBF (the full side view of the snapshot with ice growth near the IBF of the protein can be found in Fig. S12). The formation of a hexagonal ice-like structured hydration layer can be attributed to the synergetic effects of the regular arrangement of hydrophobic methyl groups (cyan–white spheres in Fig. 4 *A* and *B*) and hydrophilic hydroxyl groups (red–white spheres) of the residues on the IBF consisting of a flat β-sheet array. Moreover, the average distance between the oxygen atom of the hydroxyl groups in threonine residues is almost a constant of 4.6 Å, which is very close to the lattice constant of the ice crystals. Interestingly, we found five trapped water molecules (magenta–white sticks) between two threonine arrays. Each trapped water molecule on average forms 1.7 hydrogen bonds with the adjacent hydroxyl groups on the IBF; and at the same time, it forms on average 1.9 hydrogen bonds to the ice-like water molecules atop. Therefore, these trapped water molecules are the key intermediate for the formation of the hexagonal ice-like hydration layer atop the IBF, linking the IBF and the hexagonal ice-like hydration layer through hydrogen bonding.

In sharp contrast, the water molecules of the hydration layer atop the NIBF of one trajectory show disordered structure and almost no hexagonal ice-like structure can be observed (Fig. 4 *C* and *D*). On the NIBF, irregular arrangement of hydrophobic/hydrophilic groups and the existence of bulky hydrophobic groups and charged groups lead to the disordered structure. Depending on previous reports (35, 39, 40), the fraction of ice-like water molecules determines ice nucleation. This means that the IBF with hexagonal ice-like structured hydration layer promotes ice nucleation and the NIBF with disordered hydration layer depresses ice nucleation (41, 42), which are consistent with our experimental observations. Similar hexagonal ice-like water molecules of the hydration layer atop the IBF and disordered water molecules atop the NIBF of *Mpd*AFP were observed in our MD simulation (Fig. S13).

We further calculated the normalized hydrogen bond number on average of three trajectories formed between the side chain of all of the residues and the water molecules, when the IBF or NIBF of the *Tm*AFP is in contact with ice or supercooled liquid water (Fig. 4*E* and details in *Computational Methods*). To achieve this result, the systems with the AFP solvated in the supercooled liquid water without ice were also designed (Fig. S11*C*). Here, the normalized hydrogen bond number is defined as N/N_{max}, where N and N_{max} are the calculated number of hydrogen bonds formed and the maximum number of hydrogen bonds could form between the side chains of the residues on IBF ($N_{max} = 20$) or NIBF ($N_{max} = 32$) and water molecules. On the IBF of the *Tm*AFP, the normalized

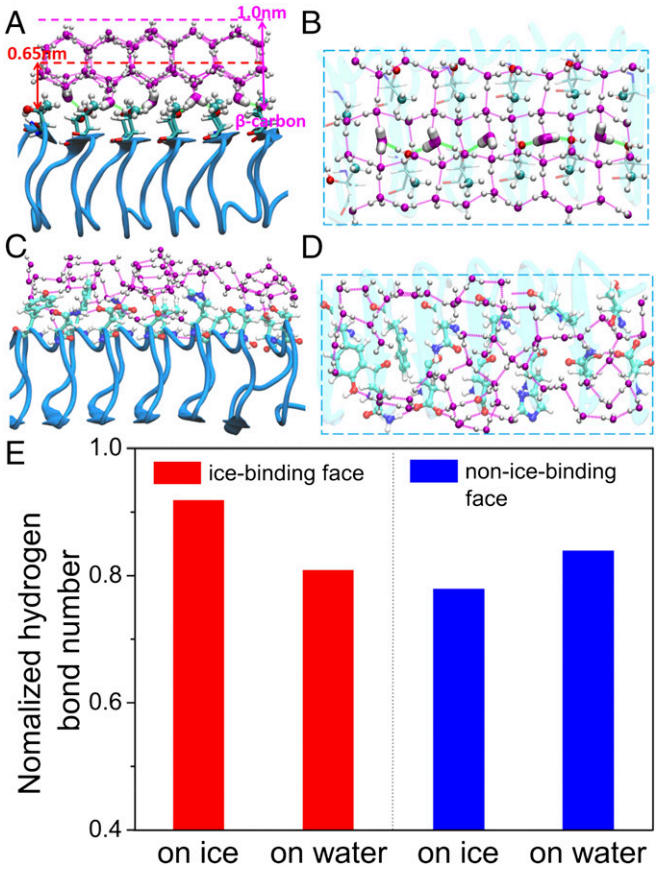

Fig. 4. Molecular level mechanism of AFPs in tuning ice nucleation. (*A*) Side view and (*B*) top view of the hexagonal ice-like water molecules (magenta–white spheres), including the trapped water molecules (magenta–white sticks) atop the ice-binding face with the methyl (cyan–white spheres) and hydroxyl (red–white spheres) groups. The water molecules displayed are located within the rectangular area of the four marginal lines for the residue atoms in the *x* and *y* directions, confirming the distance between the β-carbon atom of the 12 selected residues on the IBF or NIBF and any atom of water molecules $D \leq 0.65$ (for *A*, the cutoff value is set as 1.0 nm). For the IBF, we selected residues Ala-14, Thr-16, Thr-26, Thr-28, Thr-38, Thr-40, Thr-50, Thr-52, Thr-62, Thr-64, Ala-74, and Thr-76. (*C*) Side view and (*D*) top view of disordered waters atop the non–ice-binding face (carbon, nitrogen, oxygen, and hydrogen atoms are represented in cyan, blue, red, and white spheres). For the NIBF, we selected residues Asp-7, Thr-9, Asn-20, Pro-22, His-32, Val-34, Asp-44, Asn-46, Asp-56, Phe-58, Asn-68, and Tyr-70. (*E*) Normalized hydrogen bond number between ice/supercooled liquid water and the ice-binding face or the non–ice-binding face.

hydrogen bond number with ice is 0.92, which is larger than that with the liquid water (0.81), whereas on the NIBF, the normalized hydrogen bond number with ice is 0.78, which is less than that with liquid water (0.84). Obviously, it reveals that the hexagonal ice crystal is energetically more stable on the IBF, whereas disordered liquid water is energetically more stable on the NIBF. It agrees well with our ATR-FTIR investigation as shown in Fig. 1*D*, *Insets*. This finding further confirms that the IBF can facilitate ice nucleation and NIBF can depress ice nucleation.

Discussion

Unlike selective surface tethering in this study, the AFPs are freely distributed in body fluids and tissues of organisms. Therefore, both IBF and NIBF would be exposed in the organisms' inner environment in practical situations. That is, when the IBF of an AFP binds to the ice crystal surface or adsorbs onto nucleation active sites, the NIBF is exposed to liquid water. A natural question is what would be the effect of the NIBF on the growth or nucleation

of ice in supercooled condition. It seems that the role of the NIBF has been neglected in previous reports (4). Our experiments show that the NIBF can depress the formation of ice nuclei, and the NIBF of AFPs with a higher activity of TH exhibits higher activity in depressing ice nucleation. This finding may provide another explanation for various capabilities of different AFPs in depressing the freezing point, which was attributed to the binding of the AFPs to different crystal faces (20, 43, 44). All these findings show that both the IBF and the NIBF of AFPs are important, and they cooperatively work together rendering the AFPs having the capability of protecting living organisms at subzero conditions. The proper function of AFPs in inhibiting the growth of ice crystals and suppressing ice nucleation relies on the adsorption and inhibition function of AFPs, which is realized only through the synergetic function of both IBF and NIBF. IBF binds to the ice crystal or ice nucleator surface, leaving the NIBF exposed to liquid water (45); and the NIBF can suppress the ice nucleation or further growth of ice crystals (46). Moreover, previous contradictory observations about the effect of AFPs on ice nucleation can be rationalized since our work shows that AFPs exhibit the Janus effect on ice nucleation.

Understanding and controlling of ice nucleation influences our everyday life as well as other fields such as climate science, geoscience, and cryobiology. Our work has great implications for the understanding and controlling of ice nucleation. Our experiments show that only when synergetic cooperation of specific spatial arrangement of methyl groups (hydrophobic) and hydroxyl groups (hydrophilic) can lead to a pronounced promotion of ice nucleation (in the case of *Mpd*AFP and *Mp*AFP), whereas arrangement of merely hydroxyl groups leads to a modest or no obvious promotion of ice nucleation (type III AFP). These results obviously show that hydrophobicity is not the criterion for predicting the heterogeneous ice nucleation capacity of a surface, which is also recently suggested by some theoretical research groups (35, 47, 48). In combining with the MD simulation analysis, our work shows that the structure of interfacial water atop a specific solid surface, i.e., if it can facilitate the epitaxial growth of ice crystals, may be a good criterion for predicting the ice nucleation capability of this surface. From materials scientists' point of view, our work displays that specific arrangement of methyl groups and hydroxyl groups leads to surfaces with an enhanced heterogeneous ice nucleation capability, whereas the introduction of bulky hydrophobic groups and charged groups results in surfaces with a depressed heterogeneous ice nucleation capability. As such, this work will also guide materials scientists in the synthesis of surface materials in tuning ice nucleation.

Materials and Methods

Proteins and Chemical Materials. *Mpd*AFP was expressed and purified as previously described (18). *Mp*AFP and type III AFP were kindly provided by Peter L. Davies, Queen's University, Kingston, Ontario, Canada. *Mpd*AFP and type III AFPs were diluted by 20 mM Tris·HCl (pH = 8); *Mp*AFP was diluted with 20 mM Tris·HCl (pH = 8) and 2 mM $CaCl_2$. The purity of AFPs was investigated by SDS/PAGE (Fig. S1). Dopamine hydrochloride (DA-HCl), GOPTS, Tween-60, and Tween-20 were purchased from J&K Scientific.

TH Activity of Antifreeze Proteins. TH measurements were performed with an Otago nanoliter osmometer. First, a six-well sample holder was filled with immersion oil (viscosity = 1,250 cSt). The sample solution was injected into the oil with a nanoliter volume. Then the sample holder was placed on the thermal control stage, which was fixed on the optical stage of the microscopy (Olympus, BX51) for observing the sample in a transmission mode. When the freeze mode of the device was switched on, the temperature of the sample holder decreased quickly and the droplet was totally frozen. After that, the run mode of the device was switched on, the temperature increased slowly until a single ice crystal was left in the droplet, and it recorded the temperature at which the ice crystal stop melting as T_m. Then the temperature was decreased in a rate of 0.01 °C/s and recorded the temperature rendering the ice crystal growth spontaneously as T_f. The difference between T_m and T_f is the TH value. The ice crystal shaping and the sudden burst phenomenon appear when the solution contained AFPs.

AFP Immobilization and Characterization. Silicon substrates with a size of 5.0 × 5.0 mm^2 (N type, <100> oriented) were sequentially ultrasonically rinsed in ethanol, acetone, and Ultrapure water (Milli-Q; 18.2 MΩ/cm), and then dried under a nitrogen stream. Oxygen plasma (100 W, 120 S) treatment was applied to enrich hydroxyl groups on the substrates. PDA-modified surfaces were obtained by dipping the cleaned silicon substrates to the fresh DA-HCl solution (20 mM Tris·HCl pH = 8.5) purged with a pure oxygen flow for 20 min as described in a previous report (22). Then NIBF surfaces with various normalized coverage were obtained by dipping PDA surfaces into the AFP buffer solution (20 mM Tris·HCl, pH = 8, 0.5 wt% Tween-60) with immersion time varying from 2 to 24 h, and then rinsed with buffer solution (20 mM Tris·HCl, pH = 8, 0.5 wt% Tween-20) in a vortex mixer three times and rinsed with 20 mM Tris·HCl buffer three times, then rinsed with Ultrapure water (Milli-Q; 18.2 MΩ/cm) three times. Tween-60 and Tween-20 were used for enhancing specific reactions and restraining nonspecific adsorption of proteins as described (49). GOPTS surfaces were obtained by placing the cleaned silicon substrates in a desiccator together with 200 μL GOPTS. The desiccator was vacuum evacuated and kept for 1 h at 140 °C for the vapor phase deposition and 5 h at 175 °C for cross-linking on the surfaces. After ultrasonic rinsing in ethanol, the GOPTS surfaces were coated with AFPs by immersing the substrate in the AFP buffer solution (20 mM Tris·HCl, pH = 8, 0.5 wt% Tween-60) with duration ranging from 5 min to 2 h to get different IBF surfaces with various surface coverage. The rinsing procedure is the same as that for treating the NIFB surfaces as described above.

The AFM images were obtained from Multimode 8 (Bruker). Contact angles (CAs) of water drops were tested at room temperature with DSA100 (Krüss). The chemical compositions of the surfaces were characterized by XPS (ESCALab220i-XL). The ATR-FTIR was performed by Vertex 80 (Bruker). A silicon ATR crystal was coated with PDA, PDA-AFPs, GOPTS, and GOPTS-AFPs using the same protocols as those for the preparation of AFP-coated silicon surfaces.

Ice Nucleation Measurement. The ice nucleation temperature and delay time were investigated in a closed cell with a volume of 0.283 cm^3 (a cylinder shaped cell with a height of 2.5 mm and a diameter of 12 mm) and the closed cell was placed atop a cryostage (Linkam THMS 600). Inside the closed cell, six water droplets (each with a volume of 0.1 μL) were placed atop the AFPs modified surfaces to ensure 100% relative humidity as described in our previous publication (40). For obtaining the delay time, we fixed the surface temperature and recorded the time needed for the nucleation to occur. Because the volume of the closed cell is small enough, the water droplet thermodynamically equilibrates with the water vapor in the closed cell. In such an experimental condition, the relative humidity is 100%. All of the sample cell preparation was conducted in a class II type A2 biosafety cabinet. Then the sample cell was placed on the cooling stage (Linkam THMS 600) and cooled in a cooling rate of 5 °C/min. The freezing of droplets was observed through a microscope (Olympus, BX51) equipped with a high-speed CMOS camera system (Phantom V7.3). Droplets on around 100 different individual locations for each type of sample were tested. Each droplet was repeated "cooling down-ice formation and then heating up-ice melting" three times, with which we obtained the average ice nucleation temperature on each individual location.

Computational Methods. Two series simulation systems contain a *Tm*AFP (Protein Data Bank: 1EZG) solvated in the water with the IBF and NIBF deposited above the ice (111) face. The box with the size of 6.624 nm × 8.127 nm × 10 nm contains 3,888 ice molecule crystals and ~6,000 free-water molecules (Fig. S11). In the simulation systems, two counter ions are added to neutralize the systems. The simulation was carried out using the step of 1 fs with Gromacs-4.5.4 (50) in the canonical ensemble under constant volume and temperature (NVT) with a velocity-rescale thermostat at a temperature of 250 K. The OPLSAA (optimized potentials for piquid simulations all atom) force field and TIP4P/Ice (51) model were used for the protein and water molecules, respectively. Initially, the protein molecules with their IBF and NIBF in parallel with the ice and the minimal distance of the protein to the ice is about 1.2 nm. For the energy minimization process, the protein molecules are fixed and the water molecules energy minimized for 1,000 steps with the steepest descent algorithm. Then the systems were equilibrated for 300 ps with the protein fixed, and another three independent 200-ns simulations with the IBF and NIBF of proteins deposited above the ice, respectively, were performed. During the last 100-ns simulation, we position restrained four heavy atoms of the IBF or NIBF of the protein with the spring constant 100 kJ $mol^{-1}·nm^{-2}$ in three directions to mimic the experiments with the IBF and NIBF restrained by the PDA and GOPTS, respectively. As a contrast system, the *Tm*AFP protein was solvated in the 3,777 water molecules but without bulk ice at the same temperature of 250 K. After the energy minimization process and 300 ps relaxation, 50-ns simulations were performed with three independent trajectories. All of the data were collected during the last 20 ns of all of the simulations. The Lennard–Jones interactions were treated with a

cutoff distance of 1.0 nm, and the particle mesh Ewald (PME) method with a real-space cutoff of 1.0 nm was used to treat the long-range electrostatic interactions. We adopted a standard criterion for hydrogen bonds (32) (i.e., a donor–acceptor distance of 3.5 Å and a H–D–A angle of less than 30°). The hydrogen bonds formed between the water molecules adjacent to the protein and the residues near the IBF and NIBF were calculated. Note that we have excluded the main chain atoms, such as carbonyl groups and secondary amines that can also form hydrogen bonds with water. For the IBF, we selected the residues Ala-14, Thr-16, Thr-26, Thr-28, Thr-38, Thr-40, Thr-50, Thr-52, Thr-62, Thr-64, Ala-74, and Thr-76, whereas for the NIBF, we selected the residues Asp-7, Thr-9, Asn-20, Pro-22, His-32, Val-34, Asp-44, Asn-46, Asp-56, Phe-58, Asn-68, and Tyr-70. The simulation results of the *Mpd*AFP, which was created from a homology model of *Tm*AFP using the SWISS online structure prediction tool (52), can be found in Fig. S13.

ACKNOWLEDGMENTS. We thank Prof. Peter L. Davies from Queen's University for providing us *Mp*AFPs and type III AFPs and Prof. P. L. Davies, Dr. P. Ball, Prof. J. Zhao, Prof. B. Du, Prof. Y. Gao, Prof. Y. Tu, and Dr. Z. Yang for constructive discussion. Financial support was provided by the National Natural Science Foundation of China (NSFC) (Grants 51436004, 21421061, 11290164, 11204341, and U1532260), the Strategic Priority Research Program of the Chinese Academy of Sciences (CAS) (Grant XDA09020000), and the 973 Program (2013CB933800), the Key Research Program of CAS (Grant KJZD-EW-M03), the Youth Innovation Promotion Association CAS, Shanghai Supercomputer Center of China, Computer Network Information Center of CAS, National Supercomputing Center in Shenzhen (Shenzhen Cloud Computing Center), and the Special Program for Applied Research on Super Computation of the NSFC-Guangdong Joint Fund (second phase).

1. Jia Z, Davies PL (2002) Antifreeze proteins: An unusual receptor-ligand interaction. *Trends Biochem Sci* 27(2):101–106.
2. Yeh Y, Feeney RE (1996) Antifreeze proteins: Structures and mechanisms of function. *Chem Rev* 96(2):601–618.
3. Meister K, et al. (2015) Investigation of the ice-binding site of an insect antifreeze protein using sum-frequency generation spectroscopy. *J Phys Chem Lett* 6(7):1162–1167.
4. Nutt DR, Smith JC (2008) Dual function of the hydration layer around an antifreeze protein revealed by atomistic molecular dynamics simulations. *J Am Chem Soc* 130(39):13066–13073.
5. Raymond JA, DeVries AL (1977) Adsorption inhibition as a mechanism of freezing resistance in polar fishes. *Proc Natl Acad Sci USA* 74(6):2589–2593.
6. Davies PL (2014) Ice-binding proteins: A remarkable diversity of structures for stopping and starting ice growth. *Trends Biochem Sci* 39(11):548–555.
7. Bar M, Celik Y, Fass D, Braslavsky I (2008) Interactions of beta-helical antifreeze protein mutants with ice. *Cryst Growth Des* 8(8):2954–2963.
8. Matsumoto M, Saito S, Ohmine I (2002) Molecular dynamics simulation of the ice nucleation and growth process leading to water freezing. *Nature* 416(6879):409–413.
9. Du N, Liu XY, Hew CL (2003) Ice nucleation inhibition: Mechanism of antifreeze by antifreeze protein. *J Biol Chem* 278(38):36000–36004.
10. Inada T, Koyama T, Goto F, Seto T (2011) Ice nucleation in emulsified aqueous solutions of antifreeze protein type III and poly(vinyl alcohol). *J Phys Chem B* 115(24):7914–7922.
11. Wilson PW, Osterday KE, Heneghan AF, Haymet ADJ (2010) Type I antifreeze proteins enhance ice nucleation above certain concentrations. *J Biol Chem* 285(45):34741–34745.
12. Esser-Kahn AP, Trang V, Francis MB (2010) Incorporation of antifreeze proteins into polymer coatings using site-selective bioconjugation. *J Am Chem Soc* 132(38):13264–13269.
13. Charpentier TVJ, Neville A, Millner P, Hewson R, Morina A (2013) An investigation of freezing of supercooled water on anti-freeze protein modified surfaces. *J Bionics Eng* 10(2):139–147.
14. Bar Dolev M, Braslavsky I, Davies PL (2016) Ice-binding proteins and their function. *Annu Rev Biochem* 85(1):515–542.
15. Perrin A, Musa OM, Steed JW (2013) The chemistry of low dosage clathrate hydrate inhibitors. *Chem Soc Rev* 42(5):1996–2015.
16. Jia Z, DeLuca CI, Chao H, Davies PL (1996) Structural basis for the binding of a globular antifreeze protein to ice. *Nature* 384(6606):285–288.
17. Liou YC, Tocilj A, Davies PL, Jia Z (2000) Mimicry of ice structure by surface hydroxyls and water of a beta-helix antifreeze protein. *Nature* 406(6793):322–324.
18. Qiu LM, Ma J, Wang J, Zhang FC, Wang Y (2010) Thermal stability properties of an antifreeze protein from the desert beetle Microdera punctipennis. *Cryobiology* 60(2):192–197.
19. Graham LA, Liou YC, Walker VK, Davies PL (1997) Hyperactive antifreeze protein from beetles. *Nature* 388(6644):727–728.
20. Scotter AJ, et al. (2006) The basis for hyperactivity of antifreeze proteins. *Cryobiology* 53(2):229–239.
21. Lee H, Dellatore SM, Miller WM, Messersmith PB (2007) Mussel-inspired surface chemistry for multifunctional coatings. *Science* 318(5849):426–430.
22. Kim HW, et al. (2013) Oxygen concentration control of dopamine-induced high uniformity surface coating chemistry. *ACS Appl Mater Interfaces* 5(2):233–238.
23. Chittur KK (1998) FTIR/ATR for protein adsorption to biomaterial surfaces. *Biomaterials* 19(4–5):357–369.
24. Chang TM, Chakrabarty S, Williams ER (2014) Hydration of gaseous m-aminobenzoic acid: Ionic vs neutral hydrogen bonding and water bridges. *J Am Chem Soc* 136(29):10440–10449.
25. Anderson A, Ashurst WR (2009) Interfacial water structure on a highly hydroxylated silica film. *Langmuir* 25(19):11549–11554.
26. Meister K, et al. (2014) Observation of ice-like water layers at an aqueous protein surface. *Proc Natl Acad Sci USA* 111(50):17732–17736.
27. Gurganus C, Kostinski AB, Shaw RA (2011) Fast imaging of freezing drops: No preference for nucleation at the contact line. *J Phys Chem Lett* 2(12):1449–1454.
28. Jung S, Tiwari MK, Poulikakos D (2012) Frost halos from supercooled water droplets. *Proc Natl Acad Sci USA* 109(40):16073–16078.
29. Gurganus CW, Charnawskas JC, Kostinski AB, Shaw RA (2014) Nucleation at the contact line observed on nanotextured surfaces. *Phys Rev Lett* 113(23):235701.
30. Pandey R, et al. (2016) Ice-nucleating bacteria control the order and dynamics of interfacial water. *Sci Adv* 2(4):e1501630.
31. Garnham CP, Campbell RL, Davies PL (2011) Anchored clathrate waters bind antifreeze proteins to ice. *Proc Natl Acad Sci USA* 108(18):7363–7367.
32. Wang C, et al. (2009) Stable liquid water droplet on a water monolayer formed at room temperature on ionic model substrates. *Phys Rev Lett* 103(13):137801.
33. Guo P, et al. (2015) Water-cooh composite structure with enhanced hydrophobicity formed by water molecules embedded into carboxyl-terminated self-assembled monolayers. *Phys Rev Lett* 115(18):186101.
34. Wang C, Zhou B, Xiu P, Fang H (2011) Effect of surface morphology on the ordered water layer at room temperature. *J Phys Chem C* 115(7):3018–3024.
35. Fitzner M, Sosso GC, Cox SJ, Michaelides A (2015) The many faces of heterogeneous ice nucleation: Interplay between surface morphology and hydrophobicity. *J Am Chem Soc* 137(42):13658–13669.
36. Sosso GC, et al. (2016) Crystal nucleation in liquids: Open questions and future challenges in molecular dynamics simulations. *Chem Rev* 116(12):7078–7116.
37. Li T, Donadio D, Russo G, Galli G (2011) Homogeneous ice nucleation from supercooled water. *Phys Chem Chem Phys* 13(44):19807–19813.
38. Koga K, Zeng XC, Tanaka H (1997) Freezing of confined water: A bilayer ice phase in hydrophobic nanopores. *Phys Rev Lett* 79(26):5262–5265.
39. Moore EB, Molinero V (2011) Structural transformation in supercooled water controls the crystallization rate of ice. *Nature* 479(7374):506–508.
40. He Z, et al. (2016) Tuning ice nucleation with counterions on polyelectrolyte brush surfaces. *Sci Adv* 2(6):e1600345.
41. Tielrooij KJ, Garcia-Araez N, Bonn M, Bakker HJ (2010) Cooperativity in ion hydration. *Science* 328(5981):1006–1009.
42. Rezus YLA, Bakker HJ (2007) Observation of immobilized water molecules around hydrophobic groups. *Phys Rev Lett* 99(14):148301.
43. Drori R, Celik Y, Davies PL, Braslavsky I (2014) Ice-binding proteins that accumulate on different ice crystal planes produce distinct thermal hysteresis dynamics. *J R Soc Interface* 11(98):20140526.
44. Drori R, Davies PL, Braslavsky I (2015) When are antifreeze proteins in solution essential for ice growth inhibition? *Langmuir* 31(21):5805–5811.
45. Celik Y, et al. (2013) Microfluidic experiments reveal that antifreeze proteins bound to ice crystals suffice to prevent their growth. *Proc Natl Acad Sci USA* 110(4):1309–1314.
46. Duman JG (2001) Antifreeze and ice nucleator proteins in terrestrial arthropods. *Annu Rev Physiol* 63(1):327–357.
47. Lupi L, Molinero V (2014) Does hydrophilicity of carbon particles improve their ice nucleation ability? *J Phys Chem A* 118(35):7330–7337.
48. Bi Y, Cabriolu R, Li T (2016) Heterogeneous ice nucleation controlled by the coupling of surface crystallinity and surface hydrophilicity. *J Phys Chem C* 120(3):1507–1514.
49. Williams RA, Blanch HW (1994) Covalent immobilization of protein monolayers for biosensor applications. *Biosens Bioelectron* 9(2):159–167.
50. Hess B, Kutzner C, van der Spoel D, Lindahl E (2008) Gromacs 4: Algorithms for highly efficient, load-balanced, and scalable molecular simulation. *J Chem Theory Comput* 4(3):435–447.
51. Abascal JLF, Sanz E, García Fernández R, Vega C (2005) A potential model for the study of ices and amorphous water: TIP4P/Ice. *J Chem Phys* 122(23):234511.
52. Schwede T, Kopp J, Guex N, Peitsch MC (2003) SWISS-MODEL: An automated protein homology-modeling server. *Nucleic Acids Res* 31(13):3381–3385.